Glacial chronology and production rate cross-calibration of five cosmogenic nuclide and mineral systems from the southern Central Andean Plateau

Lisa V. Luna [a], Bodo Bookhagen [a,*], Samuel Niedermann [b], Georg Rugel [c], Andreas Scharf [c], Silke Merchel [c]

[a] *University of Potsdam, Institute of Earth and Environmental Science, Karl-Liebknecht-Str. 24–25, 14476 Potsdam–Golm, Germany*
[b] *GFZ German Research Center for Geosciences, Telegrafenberg, 14473 Potsdam, Germany*
[c] *Helmholtz-Zentrum Dresden–Rossendorf, Bautzner Landstraße 400, 01328 Dresden, Germany*

A B S T R A C T

Glacial deposits on the high-altitude, arid southern Central Andean Plateau (CAP), the Puna in northwestern Argentina, document past changes in climate, but the associated geomorphic features have rarely been directly dated. This study provides direct age control of glacial moraine deposits from the central Puna (24°S) at elevations of 3900–5000 m through surface exposure dating with cosmogenic nuclides.

Our results show that the most extensive glaciations occurred before 95 ka and an additional major advance occurred between 46 and 39 ka. The latter period is synchronous with the highest lake levels in the nearby Pozuelos basin and the Minchin (Inca Huasi) wet phase on the Altiplano in the northern CAP. None of the dated moraines produced boulder ages corresponding to the Tauca wet phase (24–15 ka).

Additionally, the volcanic lithologies of the deposits allow us to establish production ratios at low latitude and high elevation for five different nuclide and mineral systems: ^{10}Be, ^{21}Ne, and ^{26}Al from quartz (11 or 12 samples) and ^{3}He and ^{21}Ne from pyroxene (10 samples). We present production ratios for all combinations of the measured nuclides and cross-calibrated production rates for ^{21}Ne in pyroxene and quartz for the high, (sub-)tropical Andes. The production rates are based on our ^{10}Be-normalized production ratios and a weighted mean of reference ^{10}Be production rates calibrated in the high, tropical Andes (4.02 ± 0.12 at g^{-1} yr^{-1}). These are, ^{21}Ne$_{qtz}$: 18.1 ± 1.2 at g^{-1} yr^{-1} and ^{21}Ne$_{px}$: 36.6 ± 1.8 at g^{-1} yr^{-1} (En$_{88-94}$) scaled to sea level and high latitude using the Lal/Stone scheme, with 1σ uncertainties. As ^{3}He and ^{26}Al have been directly calibrated in the tropical Andes, we recommend using those rates.

Finally, we compare exposure ages calculated using all measured cosmogenic nuclides from each sample, including 11 feldspar samples measured for ^{36}Cl, and a suite of previously published production rates.

© 2018 Published by Elsevier B.V.

1. Introduction

The southern Central Andean Plateau (CAP) is a high-altitude, internally drained orogenic plateau between the Eastern and Western Cordilleras of the Andes in northwestern Argentina (Fig. 1, e.g., Allmendinger et al., 1997). The southern CAP is referred to as the Puna and is located to the south of the Altiplano (northern CAP). Climatically it sits within the Arid Diagonal, a zone of aridity stretching from coastal Peru in the northwest to the Argentine Pampas in the southeast. Although the Puna is a critical region in the Andean climate system (e.g., Baker and Fritz, 2015), paleoclimate data is scarce.

Records of mountain glaciations provide constraints on paleoclimatic conditions, and a growing body of work has concentrated on dating glacial features in the tropical and subtropical Andes, as well as farther south in the temperate Andes (e.g., Blard et al., 2014; Zech et al., 2009), summarized in Jomelli et al. (2014). Glacial features have been documented on the Puna, but rarely directly dated (e.g., Haselton et al., 2002). Here, we present the first glacial chronology for the central Puna, using cosmogenic nuclide based surface exposure ages from moraine boulders from two volcanic complexes (Fig. 1).

An essential input for determining exposure ages is the local production rate (e.g., Balco et al., 2008). Production rates differ
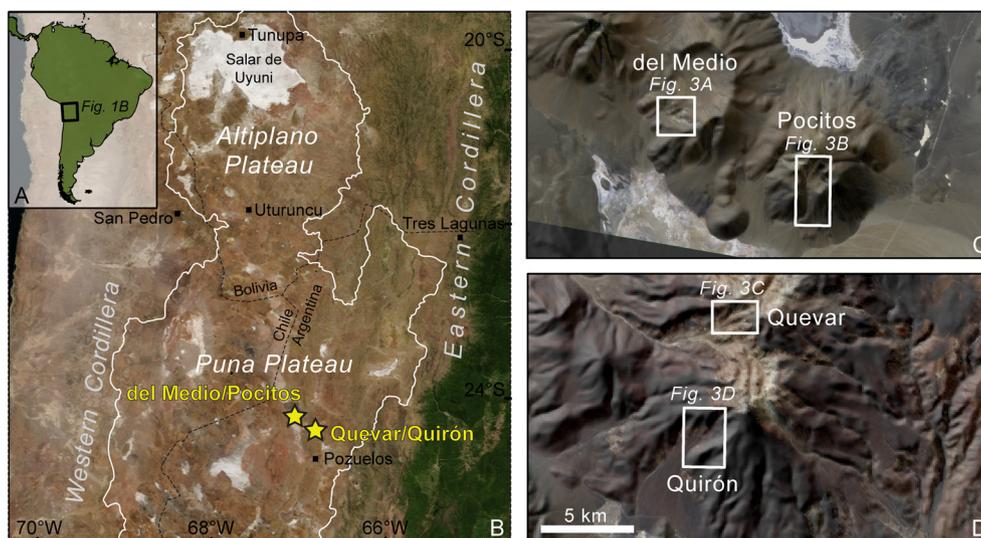
Fig. 1. Location of sampled moraines. Moraines were sampled from four different valleys on volcanoes on the Puna Plateau. (A) Location of the Puna Plateau, the arid southern extension of the internally drained central Andean Plateau. The Altiplano is the northern part of the central Andean Plateau. (B) Yellow stars show the locations of moraines sampled in this study, black squares mark other study areas mentioned in the text. White line indicates the internal drainage boundary derived from an SRTM DEM, black dashed lines are international borders. (C) Sampled valleys on Pocitos and del Medio volcanoes. (D) Sampled valleys on Quevar Volcano, which includes the Quirón site. (For interpretation of the colors in the figure(s), the reader is referred to the web version of this article.)

for each nuclide and target mineral, and also change with time, latitude, and altitude, due to the strength and geometry of the Earth's magnetic field and the thickness of the atmosphere. Therefore, estimated production rates at the study site and the resulting exposure ages depend not only on the calibration site where the reference production rate was established, but also on the scaling method, geomagnetic field history, and atmospheric model used.

One strategy to reduce uncertainty in the production rate based on the choice of scaling model is to use a calibration site that is close to the target sampling site in distance, elevation, and time (Balco et al., 2008). However, high-quality production rate calibration sites do not yet exist for all nuclides in all parts of the world (Borchers et al., 2016). Different cosmogenic nuclides are produced at a certain ratio, which may also vary geographically to a small extent. If this ratio is known, it can be combined with a locally calibrated production rate for one nuclide to calculate production rates for other nuclides (e.g., Amidon et al., 2009; Goethals et al., 2009a). The volcanic composition of the sampled boulders allows us to determine the production ratios between five different nuclide and mineral systems: ^{10}Be, ^{26}Al, and ^{21}Ne in quartz and ^{3}He and ^{21}Ne in pyroxene.

The majority of cosmogenic nuclide exposure dating studies use only one or two nuclides, based on the lithology of the samples. When considering ages calculated at different localities with different nuclides, as is often done in review studies, it is largely assumed that these ages are directly comparable (e.g., Jomelli et al., 2014). However, this assumption has seldom been tested. Our samples and nuclide combination provide the additional possibility to directly compare exposure ages calculated from six different nuclide/mineral systems from the same samples: the five listed above and ^{36}Cl from feldspar.

In summary, our study addresses three main goals: (1) Establish the first glacial chronology for the central Puna; (2) Determine production ratios between five different cosmogenic nuclide/target mineral pairings at high elevation and low latitude; and (3) Directly compare ages calculated from each nuclide system from the same sample to test the assumption that they are equivalent.

2. Geologic, climatic, and geomorphologic setting

Uplift of the CAP began between 15 and 20 Ma, with magmatism beginning during the late Oligocene (∼26 Ma) (Allmendinger et al., 1997). In the late Miocene, eruptions occurred along NW–SE striking fault systems, producing the basaltic–andesitic to dacitic del Medio, Pocitos, and Quevar volcanoes that host the moraines we sampled. These stratovolcanoes have K–Ar and Ar–Ar ages ranging between 8 and 5 Ma (Matteini et al., 2002).

Precipitation on the CAP is dominated by summer moisture brought in through the South American Monsoon System (SAMS) (e.g., Garreaud et al., 2003). The semi-arid study area receives <500 mm yr^{-1} of precipitation, at least 70% of which falls during the austral summer between December and February (DJF) (Castino et al., 2016).

The geomorphologic shapes of the studied moraines tend to be smooth, with boulder heights ranging from several tens of centimeters up to ∼2 m (Fig. 2, see Supplementary Materials for further detail). We sampled five moraines from four valleys: del Medio, Pocitos, Quirón M1 and M2, and Quevar (Fig. 3, see Figs. A1–A4 for additional detail). These range in elevation from 3900–5000 m, with the lowest moraines occurring on the del Medio and Pocitos volcanoes and the highest on Quevar (Table 1).

Moraine sequences are best preserved in the Quirón and Pocitos valleys. At Quirón, the lowest lateral moraine (M1) displays broad and flat morphology. The M2 frontal moraine stratigraphically predates the M1 moraine and is rounded. Up-valley of the M2 moraine, complex till covers the valley floor. In the Pocitos valley, hummocky terrain covers the floor of the cirque, and some small (∼2 m high) moraine features occur near the valley walls. Boulder samples from these moraines did not produce dateable material. Two rounded lateral moraines characterize the lower section of the valley – the lowest of these was dated. Farther downstream, large boulders cover an alluvial fan at the mouth of the valley and may be remnants of earlier glacial advances, but have likely been re-transported.

At del Medio and Quevar, we took a similar approach of sampling the lowest lateral moraine from the respective valleys. At Quevar, we also observed large boulders farther downstream, which, similarly to Pocitos, may be related to earlier glacial advances.
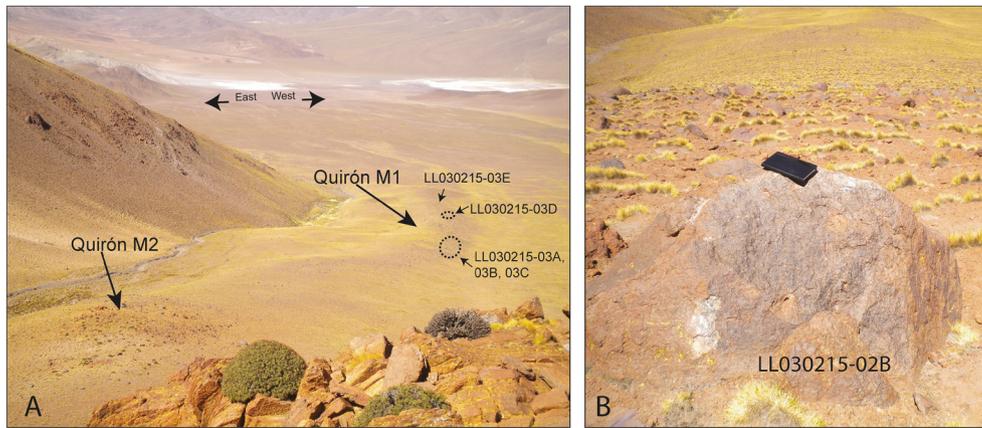
Fig. 2. Photograph of Quirón moraines and a typical boulder. The moraines are typically rounded, and boulders range from 40 cm–1.5 m in height. Care was taken to sample boulders that were well buried in the moraine material and as near to the crest of the moraine as possible. (A) Moraines at Quirón site. Dashed circles indicate the approximate locations of boulder samples on the M2 moraine. (B) Boulder LL030215-02B (Quirón M2 moraine). Field photos of all boulders are available in the Supplementary Materials.
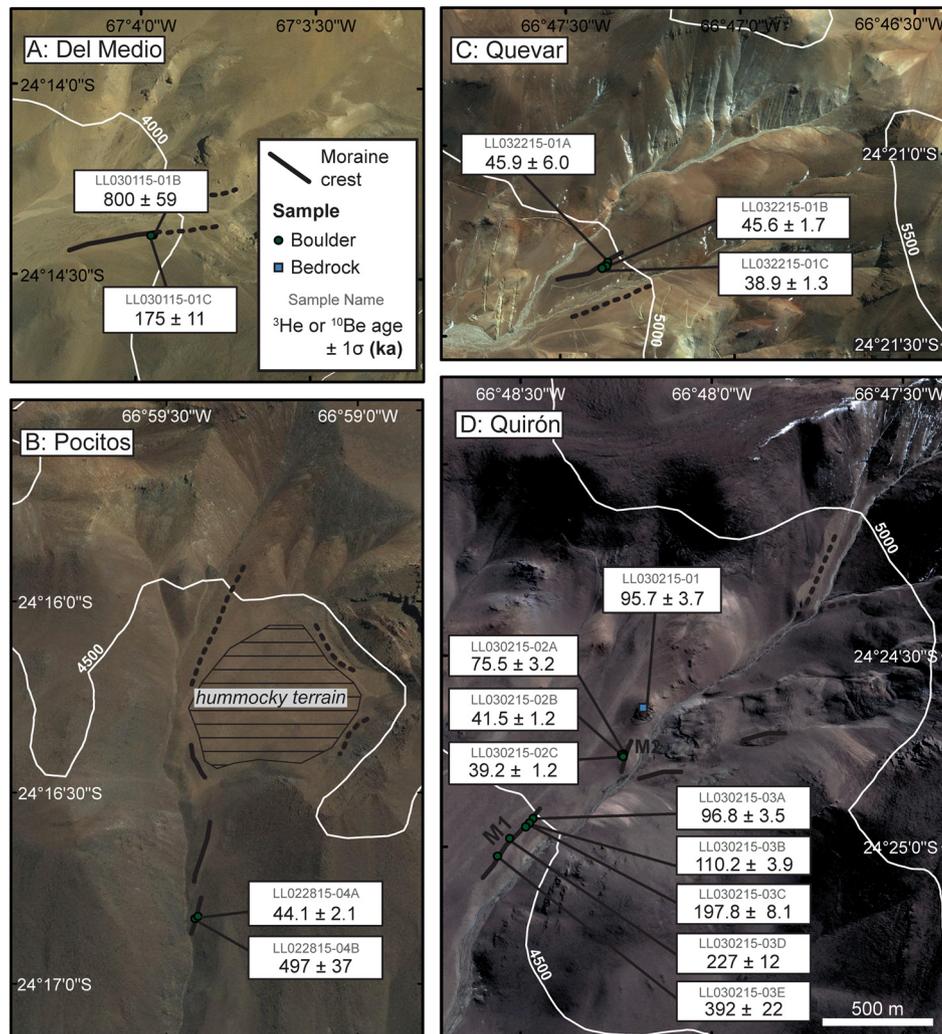
Fig. 3. Geographic context and synthesis of boulder ages (ka). Exposure ages for the sampled moraines from four different valleys are shown in ka (cf. Fig. 1, Figs. A1–A4, Table 3). All ages were calculated using CRONUScalc and Lal/Stone time dependent scaling with the default CRONUScalc geomagnetic field model and the ERA-40 atmospheric model. (A), (B) Ages for the del Medio and Pocitos sites are ^{3}He exposure ages, using a regional production rate of 130 ± 6 at g^{-1} yr^{-1} (Blard et al., 2013; Delunel et al., 2016). Uncertainties are 1σ and include analytical and production rate uncertainties. (C), (D) Ages for the Quevar and Quirón sites are ^{10}Be ages, using a production rate of 4.02 ± 0.12 at g^{-1} yr^{-1} (Kelly et al., 2015; Martin et al., 2015). White 100 m contour lines are derived from the SRTM 90 m DEM. Solid lines indicate moraines that were identified as such during field work; dashed lines indicate estimated moraines based on field observations, landform, and structure.

Table 1
General sample parameters.

Sample name	Site	Latitude (°)	Longitude (°)	Elevation asl (m)	Mean sample thickness (cm)	Density (g/cm^3)	Shielding factor[a]
LL030215-01	Quirón Bedrock	−24.41061	−66.80299	4695	3	2.59[b]	0.967
LL030215-02A	Quirón M2	−24.41263	−66.80383	4610	1.5	2.60	0.967
LL030215-02B	Quirón M2	−24.41265	−66.80392	4604	1.5	2.61	0.814
LL030215-02C	Quirón M2	−24.41275	−66.80386	4602	4	2.50	0.978
LL030215-03A	Quirón M1	−24.41544	−66.80778	4512	2.5	2.57[b]	0.931
LL030215-03B	Quirón M1	−24.41563	−66.80794	4505	5	2.57[b]	0.968
LL030215-03C	Quirón M1	−24.41574	−66.80800	4509	0.75	2.60[b]	0.897
LL030215-03D	Quirón M1	−24.41631	−66.80880	4480	5	2.63	0.978
LL030215-03E	Quirón M1	−24.41708	−66.80934	4474	1	2.62	0.977
LL032215-01A	Quevar	−24.35500	−66.78946	4991	5	2.15	0.946
LL032215-01B	Quevar	−24.35516	−66.78952	4988	3.5	2.36	0.921
LL032215-01C	Quevar	−24.35525	−66.78972	4982	0.7	2.26[b]	0.946
LL022815-04A	Pocitos	−24.28051	−66.99042	4136	3.5	2.59[b]	0.916
LL022815-04B	Pocitos	−24.28041	−66.99028	4135	5	2.59[b]	0.908
LL030115-01B	del Medio	−24.23990	−67.06596	3993	4	2.59[b]	0.895
LL030115-01C	del Medio	−24.23991	−67.06608	3997	2	2.59[b]	0.937

[a] Shielding factor includes topographic, geometric, and self-shielding.
[b] Density from a representative nearby sample or average of nearby samples.

Table 2
Nuclide concentrations (10^6 at/g) with 1σ uncertainties.

Sample name	Total ^{3}He conc.	Total ^{3}He unc.	Spallation produced ^{3}He conc.[a]	Spallation produced ^{3}He unc.[b]	^{10}Be conc.[c]	^{10}Be unc.	^{21}Ne$_{px}$ conc.	^{21}Ne$_{px}$ unc.	^{21}Ne$_{qtz}$ conc.	^{21}Ne$_{qtz}$ unc.	^{26}Al conc.[d]	^{26}Al unc.	^{36}Cl conc.[e]	^{36}Cl unc.
Mineral phase	pyroxene	pyroxene	pyroxene	pyroxene	quartz	quartz	pyroxene	pyroxene	quartz	quartz	quartz	quartz	feldspar	feldspar
LL030215-01					5.15	0.14			22.48	0.48	30.5	1.2	4.49	0.10
LL030215-02A					4.055	0.086			18.25	0.45	21.58	0.80	3.173	0.070
LL030215-02B	74.4	1.3	69.0	1.3	1.936	0.043	17.70	0.44	8.49	0.28	11.11	0.47	1.993	0.049
LL030215-02C	86.4	1.5	81.2	1.5	2.135	0.047	20.25	0.49	10.26	0.37	12.64	0.50	2.100	0.050
LL030215-03A	196.9	3.3	180.5	3.3	4.63	0.11	42.87	0.96	21.20	0.60	26.6	1.1	4.04	0.10
LL030215-03B	236.6	4.1	204.7	4.1	5.37	0.11	49.4	1.2	26.10	0.70	31.4	1.2	4.243	0.088
LL030215-03C					8.62	0.19					48.3	1.9		
LL030215-03D	375.1	6.5	352.2	6.5	9.95	0.20	89.5	2.1	42.30	0.95	55.7	2.1	8.77	0.22
LL030215-03E	548	10	512	10	14.91	0.31	138.2	3.3	66.9	1.4	88.6	3.2	11.51	0.25
LL032215-01A					2.96	0.34			13.73	0.34	13.5	3.4	3.309	0.071
LL032215-01B					2.872	0.063			12.58	0.44	17.63	0.71	2.806	0.063
LL032215-01C					2.501	0.060			11.67	0.29	14.56	0.67	2.487	0.067
LL022815-04A	64.8	1.4	59.6	1.4			14.89	0.40						
LL022815-04B	508.5	9.1	469.4	9.1			107.0	2.8						
LL030115-01B	622	11	574	11			126.8	2.7						
LL030115-01C	221.2	4.3	204.2	4.3			45.4	1.2						

[a] See sections 3.4.1 and S2 for calculation method.
[b] Uncertainty is assumed to be equal to measured ^{3}He uncertainty.
[c] ^{10}Be/^{9}Be ratios were normalized to SMD-Be-12, which has been cross calibrated to the NIST SRM 4325 standard (Akhmaldaliev et al., 2013; Nishiizumi et al., 2007).
[d] ^{26}Al/^{27}Al ratios were normalized to SMD-Al-11, which is traceable to primary standards MB04-A, MB04-B, and MB04-D (Rugel et al., 2016; Merchel and Bremser, 2004).
[e] ^{36}Cl/^{35}Cl ratios were normalized to the primary-type SM-Cl-12 standard (Merchel et al., 2011).

3. Methods and analytical results

3.1. ^{10}Be and ^{26}Al in quartz

Quartz was separated by standard mineral separation techniques. Sample purity was checked by inductively coupled plasma optical emission spectrometry (ICP-OES) (Table 2). Be and Al were extracted at Helmholtz-Zentrum Dresden–Rossendorf (HZDR) following a modified version of methods described in Merchel and Herpers (1999). We added ~300 μg of in-house ^{9}Be carrier ('Phena EA', 2246 ± 11 μg g^{-1} ^{9}Be, Merchel et al., 2013a) and ~750 μg ^{27}Al carrier (Roth Al single element standard solution for ICP, 1000.5 ± 2.0 μg ml^{-1} ^{27}Al; density = 1.011 g cm^{-3}) to the pure quartz samples before dissolution. The total Al concentration in the sample was measured from an aliquot taken after dissolution by ICP-OES at the University of Potsdam.

Be and Al isotope ratios were measured by accelerator mass spectrometry (AMS) at the DREAMS facility at HZDR (Rugel et al., 2016). ^{10}Be/^{9}Be ratios were normalized to in-house standard SMD-Be-12 (Akhmadaliev et al., 2013), which has been cross-calibrated

to the NIST SRM 4325 standard (^{10}Be/^{9}Be ratio of 2.79 ± 0.03 × 10^{-11}) (Nishiizumi et al., 2007). Al ratios were normalized to SMD-Al-11 (Rugel et al., 2016), which is traceable to primary standards (see Supplementary Text S1 for details). Measured ^{10}Be/^{9}Be ratios for the samples range from 3.40 × 10^{-13} to 2.47 × 10^{-12}, with a mean analytical uncertainty of 2.2% (1σ, $n = 11$), excluding one outlier where most of the sample was lost during chemical processing (Table A1). Measured ^{26}Al/^{27}Al ratios range from 1.01 × 10^{-12} to 1.43 × 10^{-11}, with a mean analytical uncertainty of 2.5% (1σ, $n = 11$), excluding the same outlier (Table A1). Higher uncertainties on the ^{26}Al concentrations result from propagating an estimated 3% uncertainty on the total ^{27}Al ICP-OES measurements. Blank corrections for ^{10}Be were between 0.3 and 1.4% and for ^{26}Al between 0.04 and 0.20%.

3.2. ^{36}Cl in feldspar

Feldspar was separated from whole rock samples through magnetic separation and froth floatation. ^{36}Cl extraction chemistry was performed in the ^{36}Cl laboratory at HZDR following Merchel et al.

(2013b) and Schimmelpfennig et al. (2009). After rinsing overnight with deionized water and dissolving ∼20% of the sample in an HF/HNO$_3$ solution, a solid aliquot of the grains was taken to determine the chemical composition of the feldspar. About 1.5 mg of carrier enriched in ^{35}Cl (^{35}Cl/^{37}Cl = 999) was then added to the samples before dissolution and Cl extraction.

Cl isotope ratios were measured by AMS at the DREAMS facility at HZDR. ^{36}Cl/^{35}Cl ratios were normalized to the primary-type SM-Cl-12 standard (Merchel et al., 2011). Measured ^{36}Cl/^{35}Cl ratios ranged from 4.19 × 10^{-13} to 2.00 × 10^{-12} with a mean analytical uncertainty of 2.3% (1σ, $n = 11$) (Table A2). Blank corrections ranged from 0.5 to 1.4%. The natural Cl content in the feldspars was determined by isotope dilution AMS.

To determine composition-dependent ^{36}Cl production rates, Ca, K, Ti, and Fe were measured from the feldspar separates by ICP-OES at the University of Potsdam (Table A3). Major and minor elements from the whole rock were measured by X-ray fluorescence (XRF) at the German Research Center for Geosciences (GFZ), with the exceptions of U, Th, Li, Gd, and Sm, which were measured by inductively coupled plasma mass spectrometry (ICP-MS), Cl, which was measured by ion chromatography, and H$_2$O and CO$_2$, which were measured by gas chromatography. Boron was measured by prompt gamma activation analysis (PGAA) at the Heinz Maier-Leibnitz Zentrum (Table A4). Whole rock density was determined using a pycnometer (Table 1).

3.3. ^{21}Ne in quartz

^{20}Ne, ^{21}Ne, and ^{22}Ne from the quartz separates were measured by noble gas mass spectrometry at GFZ following Niedermann et al. (1997). Gases were extracted from the samples by stepwise heating at 400 °C, 800 °C, and 1200 °C in a resistance heated furnace and He and Ne were admitted separately into the VG5400 noble gas mass spectrometer. Blank measurements had an atmospheric composition and ranged from 0.9–1.4 × 10^{-12} cm^3 STP (Standard Temperature and Pressure) for ^{20}Ne depending on temperature. Aliquots from three samples were crushed in vacuo to determine the isotopic composition of trapped Ne.

Total ^{21}Ne excesses were calculated using combined data from the 400 °C and 800 °C steps (Niedermann, 2002) and the following equation:

$$^{21}Ne_{ex} = \left[\left(\frac{^{21}Ne}{^{20}Ne} \right)_m - \left(\frac{^{21}Ne}{^{20}Ne} \right)_{tr} \right] \times {}^{20}Ne_m \qquad (1)$$

where ex = excess, m = measured, and tr = trapped, and assuming that ^{20}Ne$_{ex}$ can be ignored (Niedermann, 2002). (^{21}Ne/^{20}Ne)$_{tr}$ was taken to be 0.00304 ± 0.00013, the error-weighted mean of the crushing measurements. Two samples of the CREU-1 quartz standard gave ^{21}Ne excess values (relative to atmospheric trapped Ne) of 348.2 ± 7.4 (1σ) × 10^6 at g^{-1} and 347.5 ± 6.9 (1σ) × 10^6 at g^{-1}, in perfect agreement with the CREU-1 reference value of 348 ± 5 (1σ) × 10^6 at g^{-1} (Vermeesch et al., 2015).

Measured ^{21}Ne/^{20}Ne and ^{22}Ne/^{20}Ne ratios plot very near to the spallation line representing a two-component mix between cosmogenic and atmospheric components (Fig. A5). Cosmogenic ^{21}Ne excesses range from 8.50 ± 0.28 (1σ) to 66.9 ± 1.3 (1σ) × 10^6 at g^{-1}, with a mean analytical error of 2.7% ($n = 11$, 1σ), which is dominated by the uncertainty of the mass spectrometer sensitivity (Table A5).

3.4. ^{3}He and ^{21}Ne in pyroxene

He and Ne concentrations and isotope compositions in pyroxene were measured at GFZ. Pyroxene was separated from whole rock samples through crushing, sieving to 125–500 μm, magnetic

separation, heavy liquid separation, and finally by acid leaching inspired by Bromley et al. (2014). Samples were leached for 4–6 h in a 1% HF/1% HNO$_3$ solution in an ultrasonic bath, then checked for purity with a binocular microscope. If still substantially impure, samples were leached one or two additional times. After leaching, samples were hand-picked.

Pyroxene separates were manually crushed under vacuum to determine the trapped ^{3}He/^{4}He and ^{21}Ne/^{20}Ne ratios. After crushing, samples were sieved to >100 μm before heating to minimize the contribution of atmospheric He irreversibly adsorbed to the grains (Protin et al., 2016). However, stepwise heating measurements of both the >100 μm and <100 μm fractions of LL030215-03A after crushing yielded identical ^{3}He concentrations (Table A6), suggesting that there was no contribution of atmospheric He.

After baking at 100 °C for one week, noble gases were extracted in two heating steps at 900 and 1750 °C, purified, and measured in a Helix SFT mass spectrometer using procedures similar to those for quartz samples. During the Ne measurements, severe 'memory effects' were observed, a phenomenon where some gas ions from the current sample are lost through implantation into the mass spectrometer walls, and some previously implanted ions are released. As a result, the original isotopic ratios rapidly changed and tended toward atmospheric ratios over the course of the measurement. In order to calculate the true sample ratios, the 'memory effect' was corrected for following Goethals et al. (2009b), and the uncertainty of the correction was included in the total uncertainty. As argued by Goethals et al. (2009b), any inaccuracy arising from the memory correction would only affect the ^{22}Ne/^{20}Ne ratio, but not the ^{21}Ne/^{20}Ne ratio or the ^{21}Ne excess.

The ^{3}He/^{4}He ratio determined by crushing varies widely between samples, ranging from 0.33 × 10^{-6} to 80 × 10^{-6}, the latter value being unrealistically high for magmatic He and suggesting that some cosmogenic ^{3}He was released during crushing, though in abundances that are negligible compared to those released by heating. For stepwise heating measurements, blank values for ^{4}He ranged from 5 × 10^{-12} to 1 × 10^{-10} cm^3 STP. Blank corrected total measured ^{3}He ranged from 64.8–622 × 10^6 at g^{-1}, with a mean uncertainty of 1.8% ($n = 10$, 1σ) (Table A6). Two aliquots of the CRONUS-P pyroxene standard material were measured alongside the samples and gave ^{3}He concentrations of 4.86 ± 0.10 × 10^9 and 4.79 ± 0.10 × 10^9 at g^{-1}, which agree within 2σ uncertainties with the global mean value of 5.02 ± 0.12 × 10^9 at g^{-1} (Blard et al., 2015).

^{21}Ne$_{px}$ excesses were calculated using Eq. (1) and assuming an atmospheric ratio for trapped Ne. In many cases, ^{20}Ne concentrations were barely above blank level, which would lead to a large uncertainty from a blank correction. However, assuming that both the trapped and blank gases have atmospheric composition, the blank correction does not need to be known and will not affect the ^{21}Ne excess. ^{21}Ne/^{20}Ne and ^{22}Ne/^{20}Ne ratios for both the sample and CRONUS-P measurements plot very close to the spallation line (Fig. A5). ^{21}Ne excesses ranged from 17.70 to 126.8 × 10^6 at g^{-1}, with a mean uncertainty of 2.4% ($n = 10$, 1σ) (Table A6).

U, Th, and Li concentrations from the pyroxene crystals were determined by ICP-MS and major/minor elements were determined by ICP-OES, both at GFZ (Table A3).

3.4.1. Estimating cosmogenic ^{3}He concentrations

The total measured ^{3}He in a pyroxene sample stems from three sources: trapped ^{3}He, nucleogenic and cosmogenic thermal neutron produced ^{3}He, and spallation produced cosmogenic ^{3}He. The total measured ^{4}He in a sample is a combination of trapped ^{4}He and radiogenic ^{4}He (e.g., Niedermann, 2002). The contributions of these sources were estimated following Blard and Farley (2008); see Supplementary Text for details.

In brief, radiogenic ^{4}He (^{4}He*) produced by decay of U and Th was calculated following Blard and Farley (2008) (see Supplementary Text S2 for details). Since the U and Th concentrations in the rock matrix are in some cases up to 650 times higher than those in the pyroxene crystals, ^{4}He* implanted from the matrix is the dominant source of ^{4}He* in these pyroxene samples. Assuming a closure age for He of 8 Ma (Matteini et al., 2002), the calculated ^{4}He* concentrations turn out higher than the total measured ^{4}He concentrations for all samples except one (Table A7). The discrepancy between the calculated and measured concentrations is most likely explained by loss of material from the surface of the crystals, where implanted ^{4}He* is concentrated, through leaching.

Nevertheless, the consistently higher predicted values with respect to the measured ones suggest that the majority of ^{4}He in these samples is radiogenic. Furthermore, the concentrations of ^{4}He released by heating were often two orders of magnitude higher than those released by crushing, which is typical of samples dominated by radiogenic ^{4}He. The ^{4}He$_{tr}$ component is likely to be very small when compared with the total measured ^{4}He. It then follows that the concentration of trapped ^{3}He is also small with respect to the total measured ^{3}He. As the trapped ^{3}He concentrations are similar to the analytical uncertainty of the total measured ^{3}He concentrations, and far less than uncertainties of the resulting ages, we apply no corrections for trapped ^{3}He and assume that all measured ^{3}He is either cosmogenic or nucleogenic in origin. Doing so should have a negligible effect on the resulting production ratio or age calculations.

^{3}He produced by thermal neutron absorption by ^{6}Li was corrected for following Andrews et al. (1986). Lithium concentrations in the pyroxene samples range from 24–71 μg g^{-1}. For the contribution from cosmogenic thermal neutrons, an erosion rate of 1 mm kyr^{-1} and the ^{10}Be or ^{21}Ne$_{px}$ exposure age of the sample was used (Table A7).

After corrections, the concentrations of cosmogenic spallation produced ^{3}He range from 60–574 × 10^6 at g^{-1}, which is 87–94% of the measured ^{3}He (Table A7).

3.5. Production rates and age calculations

Using CRONUScalc Matlab codes (Marrero et al., 2016), we calculated exposure ages from all measured nuclide systems using previously published production rates to test the hypothesis that ages from the same samples are directly comparable. ^{21}Ne ages from pyroxene were calculated using a modified version of the ^{21}Ne from quartz functions. We used the time-dependent Lal/Stone (Lm) scaling model, with the default CRONUScalc v2.0 geomagnetic history, and estimated atmospheric pressure from the ERA-40 dataset (see references in Marrero et al., 2016). The attenuation length for spallation reactions was taken to be 160 g cm^{-2} (e.g., Balco et al., 2008).

Where available, we took production rates from nearby calibration sites in order to minimize the influence of the scaling and atmospheric models. For ^{3}He, we used the weighted mean of two production rates calibrated within 500 km of our study site at the Tunupa Volcano and the San Pedro Volcano (Fig. 1): 130.0 ± 6.3 at g^{-1} yr^{-1} SLHL (Blard et al., 2013; Delunel et al., 2016). For ^{10}Be, we used a tropical Andes regional production rate similar to that proposed by Martin et al. (2015) of 4.02 ± 0.12 at g^{-1} yr^{-1} SLHL, which is a combination of two independent ^{10}Be calibrations at the Azanques and Quelccaya sites (Kelly et al., 2015; Martin et al., 2015). The ^{3}He and ^{10}Be reference production rates were scaled to SLHL using the CREp website (http://crep.crpg.cnrs-nancy.fr, accessed March 4, 2016) with identical parameters as the CRONUScalc calculations (Martin et al., 2016). We combined the ^{10}Be production rate with the ^{10}Be/^{21}Ne production ratio in quartz of 0.232 ± 0.009 determined by Goethals et al. (2009a)

for a ^{21}Ne production rate in quartz of 17.33 ± 0.85 at g^{-1} yr^{-1} SLHL. Similarly, we combined the ^{10}Be production rate with the ^{26}Al/^{10}Be ratio determined at the Quelccaya site in Peru (Phillips et al., 2016) of 6.74 ± 0.34, yielding a ^{26}Al production rate of 27.1 ± 1.6 at g^{-1} yr^{-1} SLHL. As there is no local calibration for ^{36}Cl in Ca-rich minerals, we used CRONUS-Earth global reference production rates, which are 51.7 ± 4.9 at (g Ca)$^{-1}$ yr^{-1} and 151 ± 14 at (g K)$^{-1}$ yr^{-1} SLHL (Borchers et al., 2016).

For ^{21}Ne in pyroxene, we calculated composition-dependent production rates for each sample following Fenton et al. (2009). Reference production rates for each element were determined by normalizing model predicted ^{21}Ne production rates (Masarik, 2002) to a reference SLHL production rate of 46 ± 4 at g^{-1} yr^{-1} in olivine Fo$_{81}$, as found by Poreda and Cerling (1992) and rescaled using Lal/Stone time-dependent scaling (Lm).

The pyroxene samples in this study are low-calcium pyroxenes (En$_{88-94}$), with an average composition of (Ca$_{0.6}$,Mg$_{1.74}$,Fe$_{0.09}$, Ti$_{0.01}$,Mn$_{0.01}$)(Si$_{1.90}$,Al$_{0.11}$)O$_3$, which means that they have a higher Mg and a lower Ca content than pyroxenes used in previous calibrations of cosmogenic ^{21}Ne production rates (e.g., Fenton et al., 2009; Amidon et al., 2009). The calculated composition-dependent production rates for ^{21}Ne$_{px}$ range from 31.9–35.1 at g^{-1} yr^{-1} SLHL. As production rates of ^{21}Ne from Mg spallation are much higher than from Ca spallation, ^{21}Ne production rates in these samples are expected to be higher than those determined in previous studies (Masarik, 2002; Fenton et al., 2009; Amidon et al., 2009).

3.5.1. Erosion considerations

Field evidence indicated that the boulders have experienced some amount of aeolian erosion. Elsewhere on the Puna, aeolian erosion rates have been found to range between 1 and 10 mm kyr^{-1} (Bookhagen and Strecker, 2014). The highest rates were observed in unsheltered areas at ridge crests, whereas the boulder samples in this study are from relatively sheltered mountain valley bottoms. Kelly et al. (2015) found erosion rates between 1 and 5 mm kyr^{-1} for moraine boulders sampled in the Peruvian Andes, which are likely to be higher than on the Puna. These rates can unfortunately not be estimated by simultaneously solving for an exposure age and erosion rate using multiple nuclides, as the analytical uncertainty of the ratio between the nuclides in most cases overlaps a wide range of possible erosion rate and exposure age combinations (Fig. A6). We therefore consider 5 mm kyr^{-1} to be a maximum possible erosion rate, with 1 mm kyr^{-1} as a more likely estimate (see section 4.1 for discussion).

3.6. Production ratio calculations

For the production ratio calculations, decay corrections for radioactive nuclides were made using the ^{10}Be exposure age and assuming an erosion rate of 1 mm kyr^{-1} (see S3 of the Supplementary Text for details). Although ^{36}Cl was measured from feldspar for many of these samples, we do not calculate production ratios using ^{36}Cl because the high concentrations of both Ca and K in these feldspars make it difficult to attribute production to one element or the other without making further assumptions about the production rates.

4. Exposure age results and discussion

4.1. Impact of assumed erosion rate on exposure ages and production ratios

The exposure ages and production ratios presented here were calculated assuming an erosion rate of 1 mm kyr^{-1} integrated over the entire time of exposure. In reality, it is unlikely that erosion rates were steady over the entire exposure period, and more likely changed with changes in climate. Unfortunately, it is difficult to

reconstruct a record of erosion rates through time. Uncertainty in the erosion rate estimates affects older boulder ages more than younger ones. For samples with ^{10}Be exposure ages near 40 ka, as is the case for the Quevar and Quirón M2 moraine boulders, using a 5 mm kyr^{-1} erosion rate instead of a 1 mm kyr^{-1} rate makes the ages around 15% older (6 kyr). However, for boulders with a ^{10}Be exposure age of 95 ka, the ages become 60%, or 50 kyr, older. The oldest boulders reach steady-state conditions with respect to ^{10}Be. Thus, uncertainty on erosion rate estimates does not change the paleoclimatic interpretations for the younger moraines (40 ka), but may have an impact on the older exposure ages.

Production ratios are much less sensitive to changes in erosion rate than exposure ages. For ^{10}Be/^{21}Ne$_{qtz}$, for example, for samples with ^{10}Be exposure ages of around 40 ka, using an erosion rate of 5 mm kyr^{-1} instead of 1 mm kyr^{-1} results in an increase in the production ratio of 0.09%. For samples with exposure ages of around 90 ka, this increases only to 0.7%. As this is smaller than the analytical uncertainty, we can conclude that uncertainty in the erosion rate is not a major source of uncertainty in the production ratio determination. We do note, however, that for some nuclide pairs involving one stable and one radioactive nuclide, the production ratio shows a slight correlation with exposure age (Fig. 4).

4.2. Moraine ages

Exposure ages were calculated for a total of 15 boulders from five moraines and one bedrock sample (Fig. 3, Table 3). We consider the ^{10}Be ages to be the most reliable, as the production rate is well constrained in the tropical Andes and the production mechanisms for ^{10}Be are relatively simple. Where ^{10}Be was not measured, we use the ^{3}He age. The samples for which radioactive nuclides were measured show no evidence of pre-exposure and burial (Fig. A6).

The Quevar and Quirón M2 moraines have similar boulder exposure ages clustering between 39 and 46 ka, with one outlying older age of ∼76 ka on the Quirón M2 moraine (Fig. 3). We reject this age because the particularly angular boulder likely represents a pre-exposed fallen block from which little material was eroded during transport.

The glaciers in the valleys where we sampled moraines were likely small, and thus of limited erosive power. In such a setting, it is more likely that pre-exposure influences the distribution of boulder ages than in valleys with large glaciers. Indeed, other studies of glacier chronologies from the Andes have found widely scattered boulder ages, and concluded that pre-exposure influenced the distribution (Blard et al., 2014 and references therein).
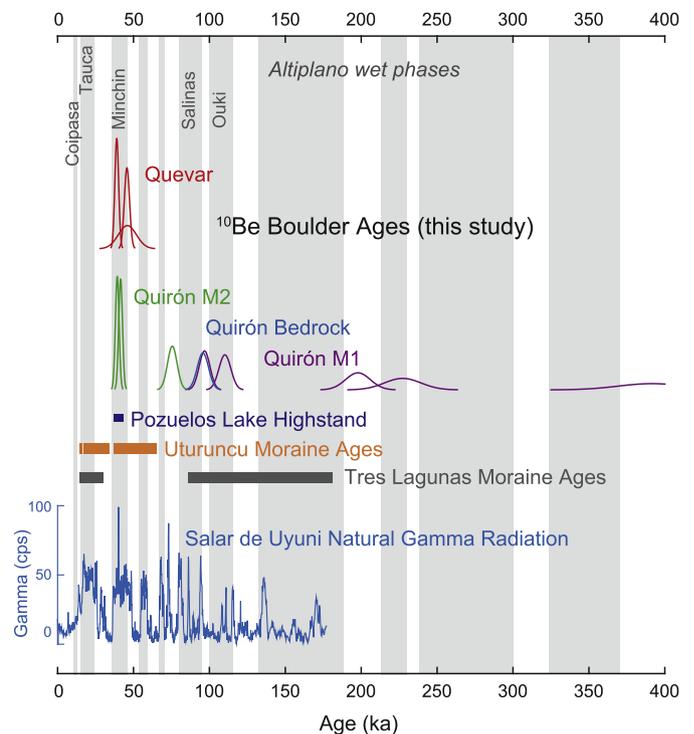
Fig. 4. Comparison of moraine boulder ages with climate proxies. The gray, shaded bars indicate documented wet phases on the Altiplano (Fritz et al., 2004, 2007; Placzek et al., 2006). ^{10}Be exposure ages and uncertainties from boulders on the Quevar, Quirón M2, and Quirón Ml moraines, and the Quirón bedrock sample are represented as probability density plots. Ages from the Quevar and Quirón M2 moraines correlate with the Pozuelos Lake highstand (McGlue et al., 2013) and the maximum glaciation at the Uturuncu Volcano (Blard et al., 2014). The youngest ages from Quirón Ml and the bedrock sample agree with moraine ages from the Tres Lagunas site in the Sierra de Santa Victoria (Zech et al., 2009). High natural gamma radiation from the Salar de Uyuni indicates wet periods on the southern Altiplano Plateau (Fritz et al., 2004).

The boulder ages for the Quirón M2 and M1 moraines agree with the stratigraphic order of the moraines. Notably, the ages of the boulders from the M1 moraine increase with distance down-valley from the top of the moraine from 97 to 392 ka. The character of the moraine also changes down-valley: from boulders with many large cobbles at the higher end to boulders with small cobbles and pebbles at the lower end, suggesting that the lower end has been weathered over a longer time period. Combining this qualitative evidence with the surface exposure ages, we suggest

Table 3
Ages (ka) from all nuclide systems with 1σ uncertainties.

Sample name	^{3}He age	^{3}He age unc.	^{10}Be age	^{10}Be age unc.	^{21}Ne$_{qtz}$ age	^{21}Ne$_{qtz}$ age unc.	^{21}Ne$_{px}$ age	^{21}Ne$_{px}$ age unc.	^{26}Al age	^{26}Al age unc.	^{36}Cl age	^{36}Cl age unc.
LL030215-01			95.7	3.7	95.3	4.8			85.1	7.1	98.4	7.7
LL030215-02A			75.5	3.2	78.2	4.9			59.6	4.4	88.3	7.9
LL030215-02B	44.9	2.2	41.5	1.2	41.9	2.0	46.0	2.4	36.5	2.3	47.4	4.2
LL030215-02C	44.7	2.1	39.2	1.2	42.7	2.2	44.4	2.0	35.3	2.1	43.0	2.9
LL030215-03A	113.7	5.8	96.8	3.5	100.9	5.5	105.7	4.7	83.3	6.9	95.9	7.6
LL030215-03B	126.9	7.1	110.2	3.9	121.5	6.3	119.5	6.0	97.9	6.7	99.8	8.4
LL030215-03C			197.8	8.1					170	16		
LL030215-03D	241	16	227	12	211	13	229	16	191	12	251	35
LL030215-03E	380	31	392	22	369	33	380	29	356	50	404	70
LL032215-01A			45.9	6.0	49.6	3.1			33.0	7.4	46.7	3.7
LL032215-01B			45.6	1.7	46.1	2.9			42.2	2.6	46.9	4.0
LL032215-01C			38.9	1.3	41.3	1.8			34.6	2.2	38.1	2.3
LL022815-04A	44.1	2.1					44.8	2.2				
LL022815-04B	498	37					443	37				
LL030115-01B	800	59					659	71				
LL030115-01C	175	11					154.2	9.7				

Ages were calculated using Lal/Stone time dependent scaling (Lm) and assuming an erosion rate of 1 mm/kyr.

that the moraine does not represent a single depositional event, but was likely reoccupied several times over its history. However, without additional analysis, for example geophysical observation of internal moraine structure, it is impossible to tell if each boulder represents a separate event, or whether boulders were re-transported or turned during subsequent events. We thus refrain from assigning an age to each advance. We argue that there were likely several glacial advances between 97 and 392 kyr, but cannot resolve the exact timing when they occurred.

The single bedrock sample at the Quirón site gives an exposure age of 96 ka, in good agreement with the youngest age of the Quirón M1 moraine. The sample is from a ridge 85 m of elevation higher than the highest sample. This may suggest that the bedrock was significantly eroded during one of the M1 depositional episodes, and exposed when the glacier retreated. It then follows that the ice was not as thick during the advance that created the M2 moraine.

The boulder ages on the del Medio (175–800 ka) and Pocitos (44.1–498 ka) moraines scatter too much to assign a depositional age and the sampling density is too low to identify outliers. However, the data still provide some useful information. The good agreement between the younger age on the Pocitos moraine of 44.1 ka and the Quirón M2 and Quevar moraines (39–46 ka) allows us to cautiously suggest that this moraine formed at a similar time. If that is the case, the other boulder age of 498 ka confirms that pre-exposure impacts the distribution of exposure ages in this area. This is further supported by the co-occurrence of exposure ages of 175 and 800 ka on the del Medio moraine.

4.3. Comparison of moraine ages with regional climate proxies

Glaciers on the Puna are thought to be aridity limited, i.e. glacier formation is more dependent on changes in precipitation than on changes in temperature (e.g., Haselton et al., 2002). Currently, the snow line increases westward across the Puna from the Eastern Cordillera to the Western Cordillera in Chile, following the trend in aridity as easterly moisture is blocked by successive ranges (Haselton et al., 2002). Previous studies have linked periods of increased moisture with glaciations on the northern CAP (Altiplano) (e.g., Blard et al., 2014; Fritz et al., 2007), and it is likely that glaciations on the Puna also indicate periods of increased precipitation.

Very little paleoclimate data exists for the Puna, whereas the Altiplano has been more widely studied. Regional paleoclimate records include sedimentary records from the Salar de Uyuni (Baker et al., 2001; Baker and Fritz, 2015; Fritz et al., 2004; Placzek et al., 2006), and a glacial chronology from the Uturuncu volcano in the southern Altiplano (Fig. 1; Blard et al., 2014). The Lake Titicaca sedimentary record from the northern Altiplano provides a longer record, but a modern precipitation gradient exists between the wetter northern and drier southern Altiplano that also may have existed in the past (Fritz et al., 2007; Placzek et al., 2006).

The most distal moraine at the Quirón site, Quirón M1, has boulders with ages increasing downslope from 97 to 392 ka (Fig. 3). The three oldest boulders on Quirón M1 are in broad agreement with interpreted phases of increased glaciation on the northern Altiplano (Fritz et al., 2007). Between 140 and 50 ka in the Salar de Uyuni record, there were multiple short perennial lake phases (Fritz et al., 2004). Evidence for a lake-level high stand between 115 and 100 ka exists in dated shorelines around Lake Poopo (termed Ouki phase) and between 95 and 80 ka around Uyuni (termed Salinas phase) (Placzek et al., 2006). The youngest two Quirón M1 ages of 110 and 97 ka, and the bedrock age of 96 ka, likely correspond to increased regional moisture associated with the Ouki and/or Salinas wet phases. At the risk of over-interpreting single boulder ages, we can therefore broadly conclude that the depositional events that formed Quirón M1 were likely in phase with documented periods of increased moisture on the Altiplano.

In the Eastern Cordillera, at the Tres Lagunas site in the Sierra de Santa Victoria (Fig. 1), Zech et al. (2009) found boulder ages on the most distal moraine between 181 and 86 ka (ages recalculated for comparison with this study). These ages are in good agreement with the younger Quirón M1 ages. Together, they suggest that the most extensive glaciation in the Eastern Cordillera and the Puna pre-dates the documented Tauca and the Minchin wet phases and related glacial advances on the Altiplano (Fritz et al., 2004).

Fig. 5 shows that boulder ages from the Quirón M2, Quevar, and Pocitos moraines ranging from 46 to 39 ka do correlate with the documented Minchin (46–36 ka, also termed Inca Huasi) wet phase on the Altiplano (Fritz et al., 2004). Glaciers were also active on the Altiplano during this time: the lowest moraine on the Uturuncu volcano in the southern Altiplano is characterized by boulders ranging from 37–65 ka, with a mode of 40 ka (Blard et al., 2014), in excellent agreement with the ages from Quirón M2 and Quevar. Sedimentological evidence from the Pozuelos Basin, just ∼30 km south of the Quirón site, suggests that the basin hosted the deepest lake between 43 and 37 ka (McGlue et al., 2013). The age concordance between the boulder ages and the Pozuelos lake record provides strong evidence for a wet phase on the Puna with glacial advances between 46 and 39 ka (Fig. 5). This is supported by observations of a wet Minchin phase that led to increased landsliding frequency (Trauth et al., 2003) and higher lake levels (Bookhagen et al., 2001) in the Eastern Cordillera just to the east of the study area.

None of the dated moraines produced boulder ages corresponding to lake-level high stands on the Altiplano during the Tauca or Coipasa wet phases, dated to 24–15 ka and 13–11 ka, respectively (Baker et al., 2001). Moraine boulders of this age have been dated both on the Altiplano (Blard et al., 2014) and in the Eastern Cordillera (Zech et al., 2009). However, in agreement with our findings, there is no evidence for either the Tauca or the Coipasa wet phases in the Pozuelos sedimentary record (McGlue et al., 2013), which could suggest that the Tauca and Coipasa phases might have been weaker in the central Puna than on the Altiplano or in the Eastern Cordillera. However, we did observe smaller moraine features up-valley of the moraines that we sampled, which may correspond to the Tauca or Coipasa phases, but moraine size and preservation did not allow for sampling. Future research could focus on better constraining the Tauca and Coipasa wet phases, or absence thereof, in the central Puna.

4.4. Establishing production ratios

Decay and erosion corrected production ratios for each boulder are presented in Fig. 4 and Table A8. Error-weighted mean production ratios from all locations (4000–5000 m) and the corresponding weighted standard deviations were calculated for each nuclide pair (Table 4).

For nuclide pairs involving one stable and one radioactive nuclide, the production ratio shows a correlation with exposure age for the two oldest samples (Fig. 4). This correlation is difficult to explain but is unlikely to be caused by an incorrect estimation of erosion rates (section 4.1). An alternative explanation could be diffusion of ^{3}He and ^{21}Ne over the long exposure periods of these boulders (227 and 392 ka). There is no significant correlation between exposure age and production ratio in the samples with exposure ages less than 110 ka, and we have therefore used these samples to calculate mean production ratios.

Our mean ^{3}He$_{px}$/^{10}Be$_{qtz}$ ratio is 37.0 ± 1.1, which is higher than the previously determined mean ratio on the Altiplano of 32.4 ±
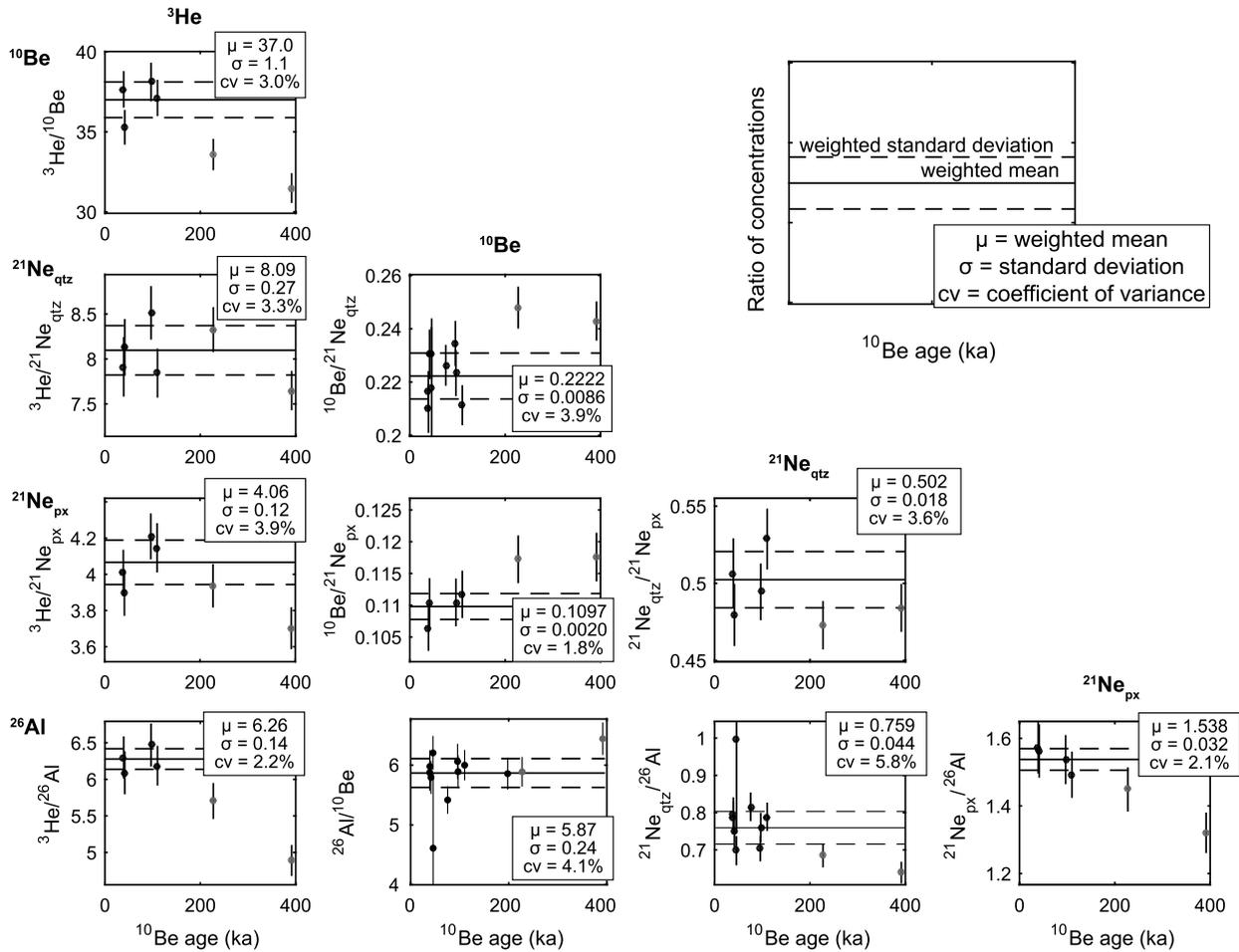
Fig. 5. Decay and erosion corrected concentration ratios. Ratios of concentrations for all possible nuclide pairings, corrected for decay and erosion for radioactive nuclides. The solid black line shows the error-weighted mean ratio of the samples and the dashed black line indicates the 1σ error-weighted standard deviation. The oldest two samples, in gray, were excluded from the weighted mean. The coefficient of variance is the weighted standard deviation divided by the weighted mean expressed as a percent, and allows spread to be compared across datasets. ^{3}He values are the concentrations of spallation-produced ^{3}He.

Table 4
Mean decay and erosion corrected production ratios.

	Production ratio	1σ standard deviation
^{3}He/^{10}Be	37.0	1.1
^{3}He/^{21}Ne$_{qtz}$	8.09	0.27
^{3}He/^{21}Ne$_{px}$	4.06	0.12
^{3}He/^{26}Al	6.26	0.14
^{10}Be/^{21}Ne$_{qtz}$	0.2222	0.0086
^{10}Be/^{21}Ne$_{px}$	0.1097	0.0020
^{26}Al/^{10}Be	5.87	0.24
^{21}Ne$_{qtz}$/^{21}Ne$_{px}$	0.502	0.018
^{21}Ne$_{qtz}$/^{26}Al	0.759	0.044
^{21}Ne$_{px}$/^{26}Al	1.538	0.032

Mean ratios of nuclide concentrations from boulders between 4000 and 5000 m. Ratios involving radioactive nuclides have been corrected for decay and erosion. ^{21}Ne$_{px}$ ratios apply to low-Ca pyroxenes like those measured in this study (En$_{88–94}$). Some of the inter-sample variation may be explained by minor differences in Mg concentration.

0.9 (Blard et al., 2014, updated in Martin et al., 2015), but still within the uncertainty range of individual boulders reported in that study.

The ^{10}Be/^{21}Ne$_{qtz}$ ratio of 0.2222 ± 0.0089 is in good agreement with the production ratio of 0.232 ± 0.009 determined by Goethals et al. (2009a) in California, and agrees within uncertainties with ratios determined above 5000 m in the Himalaya (Amidon et al., 2013). The ^{26}Al/^{10}Be ratio of 5.87 ± 0.24 is lower than the pro-

duction ratio determined by Phillips et al. (2016) of 6.74 ± 0.34 at Quelccaya in Peru (see section 4.5 for further discussion).

The ^{21}Ne$_{px}$ production rates presented here are specific to low-calcium pyroxenes with similar compositions to those measured in this study (En$_{88–94}$), as ^{21}Ne is produced from spallation of both Ca and Mg (as well as Si and Al) in pyroxene. Some of the variation in the production ratios involving ^{21}Ne$_{px}$ between samples may be explained by slight differences in Mg concentrations.

4.5. Agreement of ages between nuclide systems

We present exposure ages calculated using six different cosmogenic nuclide/mineral pairs in the same boulders and previously published production rates. Since we do not know the exposure ages of the boulders a priori, we compare the other ages to the ^{10}Be ages (Fig. 6).

The ^{26}Al ages are all younger than the ^{10}Be ages because the ratio of the production rates used to calculate the ages does not reflect the production ratio determined at this site. However, the ratios between the ages (which should be 1) do not scatter very much, meaning that if the ^{26}Al production rate were lowered by 12%, the ages would all overlap within uncertainties. An alternative explanation for the comparatively young ^{26}Al ages is that the total Al concentration ICP-OES measurements could have been systematically low, lowering the calculated ^{26}Al concentrations (e.g., Goethals et al., 2009a).
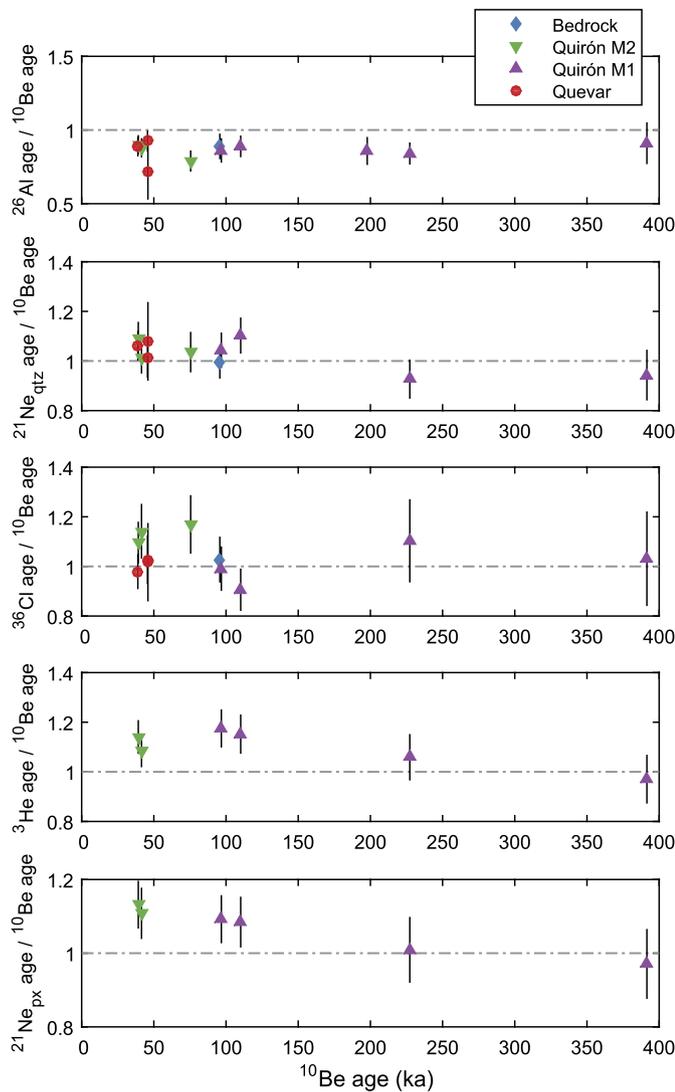
Fig. 6. Comparison of all exposure ages with ^{10}Be ages. Exposure ages were calculated with the production rates described in section 3.5. Ideally, all boulder ages would be equal, and thus have a ratio of 1, represented by the gray dotted line. As compared to ^{10}Be ages, the ^{26}Al ages are too young, and the ^{3}He and ^{21}Ne$_{px}$ ages are too old. The ^{21}Ne$_{qtz}$ ages are in excellent agreement, and the ^{36}Cl are in general agreement, although individual ages still do not agree.

The ^{21}Ne$_{qtz}$ ages and the ^{10}Be ages show very good agreement, with all ages except one agreeing within 1σ uncertainties.

The ^{36}Cl and ^{10}Be ages generally agree, but the ratios between them are more widely variable than the ratios between the ^{21}Ne$_{qtz}$, ^{26}Al, and ^{10}Be ages, meaning that for some boulders, the ages differ by more than the uncertainties. This suggests that the global CRONUS-Earth production rates for ^{36}Cl are consistent with the ^{10}Be production rates calibrated in the tropical Andes, however, the complex ^{36}Cl production mechanisms and the heightened susceptibility to production below the surface may contribute to more variability between the ages when compared with ^{10}Be ages.

The ^{3}He and ^{21}Ne$_{px}$ ages are in general slightly older than the ^{10}Be ages, with the exception of one sample. This is because the ratio of the production rates used to calculate the ages differs from the production ratio determined here, most likely because the Mg concentrations in the pyroxenes used in this study are higher than those measured in the calibration studies. Such variability between ages calculated using different nuclide systems could affect the interpretations of studies that compare ages measured with different nuclide systems.

4.6. Production rates for ^{21}Ne$_{qtz}$ and ^{21}Ne$_{px}$ in the high, tropical Andes

Using the production ratios determined in this study, and the current ^{10}Be production rate for the high, tropical Andes (Kelly et al., 2015; Martin et al., 2015), we suggest production rates for ^{21}Ne$_{qtz}$ and ^{21}Ne$_{px}$. These production rates are based on time-dependent Lal/Stone scaling as implemented in CRONUS-calc and the ERA-40 atmospheric reanalysis dataset. We find production rates of 18.1 ± 1.2 at g^{-1} yr^{-1} SLHL for ^{21}Ne$_{qtz}$ and 36.6 ± 1.8 at g^{-1} yr^{-1} SLHL for ^{21}Ne$_{px}$ (En$_{88-94}$). For ^{26}Al and ^{3}He, which have been directly calibrated in the tropical Andes, we recommend using those production rates (Blard et al., 2013; Delunel et al., 2016; Phillips et al., 2016).

5. Conclusions

This study had three major goals: (1) Develop a glacial chronology for the central Puna (southern Central Andean Plateau); (2) Determine production ratios between five different cosmogenic nuclide/mineral systems in the high elevation, (sub-)tropical Andes; and (3) Test the concordance of ages calculated using six different cosmogenic nuclide/mineral pairs in the same rock samples.

We found:

- The most extensive glaciations in the central Puna occurred >95 ka, long before the global LGM and the largest lake-level high stands on the Altiplano (northern Central Andean Plateau). An additional major advance occurred between 46 and 39 ka, synchronous with a lake high stand in the Pozuelos basin near our glacial moraine sampling sites, lake-level high stands in the Eastern Cordillera and the Minchin (Inca Huasi, 46–36 ka) wet phase on the Altiplano. None of the dated moraines produced boulder ages corresponding to the Tauca (24–15 ka) wet phase that resulted in glacial advances on the Altiplano.
- Production ratios were determined for all possible combinations of ^{10}Be, ^{21}Ne, and ^{26}Al in quartz, and ^{3}He and ^{21}Ne in pyroxene. Ratios involving ^{3}He, ^{10}Be, ^{21}Ne$_{qtz}$, and ^{21}Ne$_{px}$ tend to have the lowest spread between samples, suggesting the best internal consistency. These production ratios will allow future studies to use local calibrations of one nuclide system to determine production rates for another.
- In order for the ages calculated from two different nuclide systems to agree with each other, it is critical that the ratio of the production rates used matches the true production ratio at the site. Even when this is the case, exposure ages from two different nuclides from the same sample may not agree, particularly when the production mechanisms are complex, as for ^{36}Cl. Therefore, some caution must be used when comparing ages calculated from different nuclide systems, particularly when small differences have large impacts on paleoclimatic interpretations.

and logistical support and three anonymous reviewers for detailed comments that improved the manuscript.

Appendix A. Supplementary material

Supplementary material related to this article can be found online at https://doi.org/10.1016/j.epsl.2018.07.034.

References

Akhmadaliev, S., Heller, R., Hanf, D., Rugel, G., Merchel, S., 2013. The new 6 MV AMS-facility DREAMS at Dresden. Nucl. Instrum. Methods Phys. Res. Sect. B 294, 5–10. https://doi.org/10.1016/j.nimb.2012.01.053.

Allmendinger, R.W., Jordan, T.E., Kay, S.M., Isacks, B.L., 1997. The evolution of the Altiplano-Puna Plateau of the Central Andes. Annu. Rev. Earth Planet. Sci. 25, 139–174.

Amidon, W.H., Rood, D.H., Farley, K.A., 2009. Cosmogenic ^{3}He and ^{21}Ne production rates calibrated against ^{10}Be in minerals from the Coso volcanic field. Earth Planet. Sci. Lett. 280, 194–204. https://doi.org/10.1016/j.epsl.2009.01.031.

Amidon, W.H., Bookhagen, B., Avouac, J.P., Smith, T., Rood, D., 2013. Late Pleistocene glacial advances in the western Tibet interior. Earth Planet. Sci. Lett. 381, 210–221. https://doi.org/10.1016/j.epsl.2013.08.041.

Andrews, J.N., Fontes, J.C., Michelot, J.L., Elmore, D., 1986. In-situ neutron flux, ^{36}Cl production and groundwater evolution in crystalline rocks at Stripa, Sweden. Earth Planet. Sci. Lett. 77, 49–58. https://doi.org/10.1016/0012-821X(86)90131-7.

Baker, P.A., Fritz, S.C., 2015. Nature and causes of Quaternary climate variation of tropical South America. Quat. Sci. Rev. 124, 31–47. https://doi.org/10.1016/j.quascirev.2015.06.011.

Baker, P.A., Rigsby, C.A., Seltzer, G.O., Fritz, S.C., Lowenstein, T.K., Bacher, N.P., Veliz, C., 2001. Tropical climate changes at millennial and orbital timescales on the Bolivian Altiplano. Nature 409, 698–701. https://doi.org/10.1038/35055524.

Balco, G., Stone, J.O.H., Lifton, N., Dunai, T.J., 2008. A complete and easily accessible means of calculating surface exposure ages or erosion rates from ^{10}Be and ^{26}Al measurements. Quat. Geochronol. 3, 174–195. https://doi.org/10.1016/j.quageo.2007.12.001.

Blard, P.-H., Farley, K.A., 2008. The influence of radiogenic ^{4}He on cosmogenic ^{3}He determinations in volcanic olivine and pyroxene. Earth Planet. Sci. Lett. 276, 20–29. https://doi.org/10.1016/j.epsl.2008.09.003.

Blard, P.-H., Lavé, J., Sylvestre, F., Placzek, C.J., Claude, C., Galy, V., Condom, T., Tibari, B., 2013. Cosmogenic ^{3}He production rate in the high tropical Andes (3800 m, 20°S): implications for the local last glacial maximum. Earth Planet. Sci. Lett. 377–378, 260–275. https://doi.org/10.1016/j.epsl.2013.07.006.

Blard, P.-H., Lave, J., Farley, K.A., Ramirez, V., Jimenez, N., Martin, L.C.P., Charreau, J., Tibari, B., Fornari, M., 2014. Progressive glacial retreat in the Southern Altiplano (Uturuncu volcano, 22°S) between 65 and 14 ka constrained by cosmogenic ^{3}He dating. Quat. Res. 82, 209–221. https://doi.org/10.1016/j.yqres.2014.02.002.

Blard, P.-H., Balco, G., Burnard, P.G., Farley, K.A., Fenton, C.R., Friedrich, R., Jull, A.J.T., Niedermann, S., Pik, R., Schaefer, J.M., Scott, E.M., Shuster, D.L., Stuart, F.M., Stute, M., Tibari, B., Winckler, G., Zimmermann, L., 2015. An inter-laboratory comparison of cosmogenic ^{3}He and radiogenic ^{4}He in the CRONUS-P pyroxene standard. Quat. Geochronol. 26, 11–19. https://doi.org/10.1016/j.quageo.2014.08.004.

Bookhagen, B., Strecker, M.R., 2014. Evolution and erosional dynamics of intermontane basins on the Puna Plateau, NW Argentina. In: Am. Geophys. Union Fall Meeting, 2014. Abstr. #EP21B-3537.

Bookhagen, B., Haselton, K., Trauth, M.H., 2001. Hydrological modelling of a Pleistocene landslide-dammed lake in the Santa Maria Basin, NW Argentina. Palaeogeogr. Palaeoclimatol. Palaeoecol. 169, 113–127. https://doi.org/10.1016/S0031-0182(01)00221-8.

Borchers, B., Marrero, S., Balco, G., Caffee, M., Goehring, B., Lifton, N., Nishiizumi, K., Phillips, F., Schaefer, J., Stone, J., 2016. Geological calibration of spallation production rates in the CRONUS-Earth project. Quat. Geochronol. 31, 188–198. https://doi.org/10.1016/j.quageo.2015.01.009.

Bromley, G.R.M., Winckler, G., Schaefer, J.M., Kaplan, M.R., Licht, K.J., Hall, B.L., 2014. Pyroxene separation by HF leaching and its impact on helium surface-exposure dating. Quat. Geochronol. 23, 1–8. https://doi.org/10.1016/j.quageo.2014.04.003.

Castino, F., Bookhagen, B., Strecker, M.R., 2016. Rainfall variability and trends of the past six decades (1950–2014) in the subtropical NW Argentine Andes. Clim. Dyn. 48, 1049–1067. https://doi.org/10.1007/s00382-016-3127-2.

Delunel, R., Blard, P.-H., Martin, L.C.P., Nomade, S., Schlunegger, F., 2016. Long term low latitude and high elevation cosmogenic ^{3}He production rate inferred from a 107 ka-old lava flow in northern Chile; 22°S–3400 m a.s.l. Geochim. Cosmochim. Acta 184, 71–87. https://doi.org/10.1016/j.gca.2016.04.023.

Fenton, C.R., Niedermann, S., Goethals, M.M., Schneider, B., Wijbrans, J., 2009. Evaluation of cosmogenic ^{3}He and ^{21}Ne production rates in olivine and pyroxene from two Pleistocene basalt flows, western Grand Canyon, AZ, USA. Quat. Geochronol. 4, 475–492. https://doi.org/10.1016/j.quageo.2009.08.002.

Fritz, S.C., Baker, P.A., Lowenstein, T.K., Seltzer, G.O., Rigsby, C.A., Dwyer, G.S., Tapia, P.M., Arnold, K.K., Ku, T.L., Luo, S., 2004. Hydrologic variation during the last 170,000 years in the southern hemisphere tropics of South America. Quat. Res. 61, 95–104. https://doi.org/10.1016/j.yqres.2003.08.007.

Fritz, S.C., Baker, P.A., Seltzer, G.O., Ballantyne, A., Tapia, P., Cheng, H., Edwards, R.L., 2007. Quaternary glaciation and hydrologic variation in the South American tropics as reconstructed from the Lake Titicaca drilling project. Quat. Res. 68, 410–420. https://doi.org/10.1016/j.yqres.2007.07.008.

Garreaud, R., Vuille, M., Clement, A.C., 2003. The climate of the Altiplano: observed current conditions and mechanisms of past changes. Palaeogeogr. Palaeoclimatol. Palaeoecol. 194, 5–22. https://doi.org/10.1016/S0031-0182(03)00269-4.

Goethals, M.M., Hetzel, R., Niedermann, S., Wittmann, H., Fenton, C.R., Kubik, P.W., Christl, M., von Blanckenburg, F., 2009a. An improved experimental determination of cosmogenic ^{10}Be/^{21}Ne and ^{26}Al/^{21}Ne production ratios in quartz. Earth Planet. Sci. Lett. 284, 187–198. https://doi.org/10.1016/j.epsl.2009.04.027.

Goethals, M.M., Niedermann, S., Hetzel, R., Fenton, C.R., 2009b. Determining the impact of faulting on the rate of erosion in a low-relief landscape: a case study using in situ produced ^{21}Ne on active normal faults in the Bishop Tuff, California. Geomorphology 103, 401–413. https://doi.org/10.1016/j.geomorph.2008.07.008.

Haselton, K., Hilley, G., Strecker, M.R., 2002. Average Pleistocene climatic patterns in the southern Central Andes: controls on mountain glaciation and paleoclimate implications. J. Geol. 110, 211–226. https://doi.org/10.1086/338414.

Jomelli, V., Favier, V., Vuille, M., Braucher, R., Martin, L., Blard, P.-H., Colose, C., Brunstein, D., He, F., Khodri, M., Bourlès, D.L., Leanni, L., Rinterknecht, V., Grancher, D., Francou, B., Ceballos, J.L., Fonseca, H., Liu, Z., Otto-Bliesner, B.L., 2014. A major advance of tropical Andean glaciers during the Antarctic cold reversal. Nature 513, 224–228. https://doi.org/10.1038/nature13546.

Kelly, M.A., Lowell, T.V., Applegate, P.J., Phillips, F.M., Schaefer, J.M., Smith, C.A., Kim, H., Leonard, K.C., Hudson, A.M., 2015. A locally calibrated, late glacial ^{10}Be production rate from a low-latitude, high-altitude site in the Peruvian Andes. Quat. Geochronol. 26, 70–85. https://doi.org/10.1016/j.quageo.2013.10.007.

Marrero, S.M., Phillips, F.M., Borchers, B., Lifton, N., Aumer, R., Balco, G., 2016. Cosmogenic nuclide systematics and the CRONUScalc program. Quat. Geochronol. 31, 160–187. https://doi.org/10.1016/j.quageo.2015.09.005.

Martin, L.C.P., Blard, P.-H., Lavé, J., Braucher, R., Lupker, M., Condom, T., Charreau, J., Mariotti, V., Davy, E., 2015. In situ cosmogenic ^{10}Be production rate in the High Tropical Andes. Quat. Geochronol. 30, 54–68. https://doi.org/10.1016/j.quageo.2015.06.012.

Martin, L.C.P., Blard, P.-H., Balco, G., Lavé, J., Delunel, R., Lifton, N., Laurent, V., 2016. The CREp program and the ICE-D production rate calibration database: a fully parameterizable and updated online tool to compute cosmic-ray exposure ages. Quat. Geochronol. 38, 25–49. https://doi.org/10.1016/j.quageo.2016.11.006.

Masarik, J., 2002. Numerical simulation of in-situ production of cosmogenic nuclides. In: Goldschmidt Conference Abstracts. Geochim. Cosmochim. Acta 66, A491.

Matteini, M., Mazzuoli, R., Omarini, R., Cas, R., Maas, R., 2002. Geodynamical evolution of Central Andes at 24°S as inferred by magma composition along the Calama–Olacapato–El Toro transversal volcanic belt. J. Volcanol. Geotherm. Res. 118, 205–228. https://doi.org/10.1016/S0377-0273(02)00257-3.

McGlue, M.M., Cohen, A.S., Ellis, G.S., Kowler, A.L., 2013. Late Quaternary stratigraphy, sedimentology and geochemistry of an underfilled lake basin in the Puna Plateau (northwest Argentina). Basin Res. 25, 638–658. https://doi.org/10.1111/bre.12025.

Merchel, S., Bremser, W., 2004. First international ^{26}Al interlaboratory comparison – Part I. Nucl. Instrum. Methods Phys. Res., Sect. B 223–224, 393–400. https://doi.org/10.1016/j.nimb.2004.04.076.

Merchel, S., Herpers, U., 1999. An update on radiochemical separation techniques for the determination of long-lived radionuclides via accelerator mass spectrometry. Radiochim. Acta 84, 215–220. https://doi.org/10.1524/ract.1999.84.4.215.

Merchel, S., Bremser, W., Alfimov, V., Arnold, M., Aumaître, G., Benedetti, L., Bourlès, D.L., Caffee, M., Fifield, L.K., Finkel, R.C., Freeman, S.P.H.T., Martschini, M., Matsushi, Y., Rood, D.H., Sasa, K., Steier, P., Takahashi, T., Tamari, M., Tims, S.G., Tosaki, Y., Wilcken, K.M., Xu, S., 2011. Ultra-trace analysis of ^{36}Cl by accelerator mass spectrometry: an interlaboratory study. Anal. Bioanal. Chem. 400, 3125–3132. https://doi.org/10.1007/s00216-011-4979-2.

Merchel, S., Bremser, W., Bourlès, D.L., Czeslik, U., Erzinger, J., Kummer, N.A., Leanni, L., Merkel, B., Recknagel, S., Schaefer, U., 2013a. Accuracy of ^{9}Be-data and its influence on ^{10}Be cosmogenic nuclide data. J. Radioanal. Nucl. Chem. 298, 1871–1878. https://doi.org/10.1007/s10967-013-2746-x.

Merchel, S., Braucher, R., Alfimov, V., Bichler, M., Bourlès, D.L., Reitner, J.M., 2013b. The potential of historic rock avalanches and man-made structures as chlorine-36 production rate calibration sites. Quat. Geochronol. 18, 54–62. https://doi.org/10.1016/j.quageo.2013.07.004.

Niedermann, S., 2002. Cosmic-ray-produced noble gases in terrestrial rocks: dating tools for surface processes. Rev. Mineral. Geochem. 47, 731–784. https://doi.org/10.2138/rmg.2002.47.16.

Niedermann, S., Bach, W., Erzinger, J., 1997. Noble gas evidence for a lower mantle component in MORBs from the southern East Pacific Rise: decoupling of helium and neon isotope systematics. Geochim. Cosmochim. Acta 61, 2697–2715. https://doi.org/10.1016/S0016-7037(97)00102-6.

Nishiizumi, K., Imamura, M., Caffee, M.W., Southon, J.R., Finkel, R.C., McAninch, J., 2007. Absolute calibration of ^{10}Be AMS standards. Nucl. Instrum. Methods Phys. Res. Sect. B 258, 403–413. https://doi.org/10.1016/j.nimb.2007.01.297.

Phillips, F.M., Kelly, M.A., Hudson, A.M., Stone, J.O.H., Schaefer, J., Marrero, S.M., Fifield, L.K., Finkel, R., Lowell, T., 2016. CRONUS-Earth calibration samples from the Huancané II moraines, Quelccaya Ice Cap, Peru. Quat. Geochronol. 31, 220–236. https://doi.org/10.1016/j.quageo.2015.10.005.

Placzek, C., Quade, J., Patchett, P.J., 2006. Geochronology and stratigraphy of late Pleistocene lake cycles on the southern Bolivian Altiplano: implications for causes of tropical climate change. Bull. Geol. Soc. Am. 118, 515–532. https://doi.org/10.1130/B25770.1.

Poreda, R.J., Cerling, T.E., 1992. Cosmogenic neon in recent lavas from the western United States. Geophys. Res. Lett. 19, 1863–1866. https://doi.org/10.1029/92GL01998.

Protin, M., Blard, P.-H., Marrocchi, Y., Mathon, F., 2016. Irreversible adsorption of atmospheric helium on olivine: a lobster pot analogy. Geochim. Cosmochim. Acta 179, 76–88. https://doi.org/10.1016/j.gca.2016.01.032.

Rugel, G., Pavetich, S., Akhmadaliev, S., Enamorado Baez, S.M., Scharf, A., Ziegenrücker, R., Merchel, S., 2016. The first four years of the AMS-facility DREAMS: status and developments for more accurate radionuclide data. Nucl. Instrum. Methods Phys. Res. Sect. B 370, 94–100. https://doi.org/10.1016/j.nimb.2016.01.012.

Schimmelpfennig, I., Benedetti, L., Finkel, R., Pik, R., Blard, P.-H., Bourlés, D., Burnard, P., Williams, A., 2009. Sources of in-situ ^{36}Cl in basaltic rocks. Implications for calibration of production rates. Quat. Geochronol. 4, 441–461.

Trauth, M.H., Bookhagen, B., Marwan, N., Strecker, M.R., 2003. Multiple landslide clusters record Quaternary climate changes in the northwestern Argentine Andes. Palaeogeogr. Palaeoclimatol. Palaeoecol. 194, 109–121. https://doi.org/10.1016/S0031-0182(03)00273-6.

Vermeesch, P., Balco, G., Blard, P.-H., Dunai, T.J., Kober, F., Niedermann, S., Shuster, D.L., Strasky, S., Stuart, F.M., Wieler, R., Zimmermann, L., 2015. Interlaboratory comparison of cosmogenic ^{21}Ne in quartz. Quat. Geochronol. 26, 20–28. https://doi.org/10.1016/j.quageo.2012.11.009.

Zech, J., Zech, R., Kubik, P.W., Veit, H., 2009. Glacier and climate reconstruction at Tres Lagunas, NW Argentina, based on ^{10}Be surface exposure dating and lake sediment analyses. Palaeogeogr. Palaeoclimatol. Palaeoecol. 284, 180–190. https://doi.org/10.1016/j.palaeo.2009.09.023.